

Exploring Frequency-Domain Feature Modeling for HRTF Magnitude Upsampling

Xingyu Chen,¹ Hanwen Bi,¹ Fei Ma,¹ Sipei Zhao,^{1,a} Eva Cheng,¹ and Ian S. Burnett²

¹ Centre for Audio, Acoustics and Vibration, Faculty of Engineering and IT, University of Technology Sydney, Ultimo, NSW 2007, Australia

² Faculty of Information Technology, Monash University, Clayton, VIC 3800, Australia

(Dated: 13 February 2026)

Accurate upsampling of Head-Related Transfer Functions (HRTFs) from sparse measurements is crucial for personalized spatial audio rendering. Traditional interpolation methods, such as kernel-based weighting or basis function expansions, rely on measurements from a single subject and are limited by the spatial sampling theorem, resulting in significant performance degradation under sparse sampling. Recent learning-based methods alleviate this limitation by leveraging cross-subject information, yet most existing neural architectures primarily focus on modeling spatial relationships across directions, while spectral dependencies along the frequency dimension are often modeled implicitly or treated independently. However, HRTF magnitude responses exhibit strong local continuity and long-range structure in the frequency domain, which are not fully exploited. This work investigates frequency-domain feature modeling by examining how different architectural choices—ranging from per-frequency multilayer perceptrons to convolutional, dilated convolutional, and attention-based models—affect performance under varying sparsity levels, showing that explicit spectral modeling consistently improves reconstruction accuracy, particularly under severe sparsity. Motivated by this observation, a frequency-domain Conformer-based architecture is adopted to jointly capture local spectral continuity and long-range frequency correlations. Experimental results on the SONICOM and HUTUBS datasets demonstrate that the proposed method achieves state-of-the-art performance in terms of interaural level difference and log-spectral distortion.

[<https://doi.org/DOI number>]

[XYZ]

Pages: 1–11

I. INTRODUCTION

Head-related transfer functions (HRTFs) characterize the direction-dependent acoustic filtering of sound waves caused by the head, torso, and pinnae, and therefore serve as a fundamental component of spatial audio rendering^{1–3}. Because these structural features vary significantly across individuals, HRTFs exhibit strong person-specific characteristics⁴. Personalized spatial audio rendering requires, for each individual, HRTFs at a dense set of spatial directions⁵. However, acquiring such dense measurements is costly, time-consuming, and often impractical in real-world applications. This motivates HRTF upsampling, namely, estimating dense-direction HRTFs from a limited number of sparsely measured directions.

HRTFs encode multiple perceptual features. Interaural time difference (ITD) and interaural level difference (ILD)⁶ primarily contribute to azimuthal localization, whereas elevation perception and front-back discrimination are largely governed by frequency-dependent spectral features^{7,8}. Accordingly, many studies decom-

pose HRTF upsampling into two sub-tasks: estimating ITD and upsampling the log-magnitude spectrum, followed by minimum-phase reconstruction to obtain the time-domain impulse response, referred to as the head-related impulse response (HRIR)^{9,10}. As ITD estimation already achieves high accuracy¹¹, this work focuses on log-magnitude HRTF upsampling.

Traditional HRTF upsampling methods primarily focus on modeling spatial relationships among measured directions, following early spatial weighting and panning concepts developed for virtual sound source positioning¹². These methods can be broadly categorized into distance-weighted interpolation methods and basis function decomposition methods. The former, including bilinear interpolation¹³, spherical-triangle interpolation¹⁴, and barycentric interpolation^{15,16}, estimate target HRTFs by computing weighted combinations of neighboring measurements. The latter, such as spherical harmonic decomposition^{17–20} and spatial principal component analysis^{21,22}, represent HRTFs as linear combinations of spatial basis functions, with interpolation achieved by estimating the corresponding spatial coefficients from the measured directions. While effective under dense measurement conditions, these traditional approaches do not exploit inter-subject relation-

^asipei.zhao@uts.edu.au

ships and suffer substantial accuracy degradation under sparse sampling, as fundamentally constrained by the spatial sampling theorem.

Recent learning-based methods have improved HRTF upsampling by exploiting inter-subject relationships enabled by multi-subject datasets^{23–27}. Most existing methods are based on coordinate-based neural networks, where spatial direction is explicitly provided as an input or conditioning variable. Early works include autoencoder-based models conditioned on source direction^{28,29}, followed by neural field formulations³⁰ that represent HRTFs as continuous functions of spatial coordinates^{31–33}. Subsequent extensions incorporate explicit spatial correlation modeling using graph neural networks³⁴ or retrieval-augmented mechanisms that leverage similar subjects' HRTFs from a database, such as RANF³⁵. Alongside these methods, several studies formulate HRTF upsampling as a sparse-to-dense regression problem, directly mapping a limited set of sparse measurements to dense-direction HRTFs without explicit coordinate conditioning. Representative examples include per-frequency multilayer perceptron(MLP) models¹¹ and image-based formulations that treat direction and frequency as two-dimensional grids processed by convolutional neural networks (CNNs)³⁶. Since HRTFs are inherently defined on a spherical spatial domain, such planar grid representations do not explicitly respect the underlying geometry. Consequently, alternative spatial representations have been explored, including geometric projections³⁷, spherical CNNs^{38,39}, and spherical harmonic domain modeling^{40,41}.

Despite their effectiveness, most learning-based methods primarily emphasize spatial structure, consistent with viewing interpolation over sparsely sampled directions on the sphere. In these methods, frequency-domain information is typically handled via independent per-frequency mappings or shallow aggregation, without explicitly modeling cross-frequency structure. However, the log-magnitude spectrum exhibits rich frequency-dependent patterns, including pinna-induced resonances, spectral notches⁴², and smooth cross-frequency correlations, which remain under-exploited. Although frequency-domain components have been incorporated in several recent methods, existing results are fragmented, and the contribution of different frequency-domain modeling strategies has not been systematically examined.

Motivated by this gap, we investigate frequency-domain feature modeling for HRTF magnitude upsampling. A frequency-domain modeling design space is considered, including per-frequency multilayer perceptrons, convolutional architectures with increasing receptive fields, and attention-based models. Based on this analysis, we propose a Frequency-Domain Conformer, referred to as **FD-Conformer**, which adopts the Conformer architecture⁴³ to jointly model local spectral continuity and long-range frequency dependencies in HRTF magnitudes. Experiments on the SONICOM AND HUTUBS datasets are carried out to demonstrate the superior performance the proposed FD-Conformer

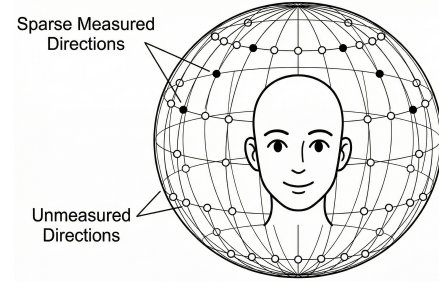


FIG. 1. Conceptual illustration of HRTF upsampling from sparse measurements.

over existing methods. The source code is available at: github.com/xingyuaudio/FD-Conformer.

II. PROBLEM STATEMENT

Figure 1 illustrates the HRTF magnitude upsampling problem considered in this work, where dense HRTFs are predicted from a limited number of sparse measurements. Let $\mathbf{d} \in \mathbb{S}^2$ denote a sound-source direction on the unit sphere, parameterized by the azimuth $\theta \in [0, 2\pi)$ and elevation $\phi \in [-\frac{\pi}{2}, \frac{\pi}{2}]$. Let $H(\mathbf{d}, e, f) \in \mathbb{C}$ denote the complex-valued HRTF from direction \mathbf{d} to the left ($e = 1$) or right ($e = 2$) ear at frequency f . It is noted that we consider far-field HRTFs, for which the dependence on source distance is negligible⁴⁴ and therefore omitted.

To generate realistic spatial audio rendering effects, the HRTFs from a dense set \mathcal{D} of source directions for a given subject are desired. In practice, however, $H(\mathbf{d}, e, f)$ is available only at a sparse subset $\mathcal{D}_M \subset \mathcal{D}$, where the cardinality $|\mathcal{D}_M| = M \ll |\mathcal{D}|$ specifies the number of measured directions.

Let $\mathcal{D}_U = \mathcal{D} \setminus \mathcal{D}_M$ denote the set of unmeasured directions, with cardinality $|\mathcal{D}_U| = U$. We focus on upsampling the log-magnitude spectrum of the HRTF, which is defined as

$$H_{\log}(\mathbf{d}, e, f) = 20 \log_{10} |H(\mathbf{d}, e, f)|, \quad (1)$$

where $|\cdot|$ denotes the magnitude operator, from the M measured directions to the U unmeasured directions.

Following the convention of learning-based methods for HRTF upsampling, we also assume access to a reference database containing densely measured H_{\log} from multiple subjects. These data provide patterns of how H_{\log} varies over direction and frequency across individuals, but only sparse measurements are available for the target subject. The goal is therefore to estimate \hat{H}_{\log} at the unmeasured directions \mathcal{D}_U for the target subject, using only the sparse measurements and the patterns learned from the reference database.

III. EXISTING METHODS

Existing methods for HRTF upsampling can be broadly categorized into traditional methods and

learning-based methods. Traditional methods estimate \hat{H}_{\log} at unmeasured directions using only the target subject's available measurements. These methods are most commonly formulated as either (i) distance-weighted interpolation schemes or (ii) decompositions onto spatial basis functions. Learning-based methods, in contrast, leverage multi-subject datasets to train neural networks that predict dense HRTFs from sparse observations.

A. Distance-Weighted Interpolation

Distance-weighted interpolation methods estimate \hat{H}_{\log} at an unmeasured direction by forming a weighted combination of the available measurements. Given sparse measurements at directions $\mathbf{d}' \in \mathcal{D}_M$, the estimate is computed as

$$\hat{H}_{\log}(\mathbf{d}, e, f) = \frac{\sum_{\mathbf{d}' \in \mathcal{D}_M} w(\mathbf{d}, \mathbf{d}') H_{\log}(\mathbf{d}', e, f)}{\sum_{\mathbf{d}' \in \mathcal{D}_M} w(\mathbf{d}, \mathbf{d}')}, \quad (2)$$

where $w(\mathbf{d}, \mathbf{d}')$ is a spatial weighting function determined by the proximity between \mathbf{d} and \mathbf{d}' . Representative examples include bilinear interpolation¹³, spherical-triangle interpolation¹⁴, and barycentric interpolation^{15,16}.

B. Basis Function Decomposition

Basis-function decomposition methods represent HRTFs as linear combinations of predefined spatial basis functions. Let $\{\Phi_n(\mathbf{d})\}_{n=1}^L$ denote a set of L spatial basis functions (e.g., spherical harmonics or principal components), and let $\mathbf{a}(e, f) \in \mathbb{R}^L$ denote the corresponding coefficient vector. The log-magnitude HRTF is modeled as

$$\hat{H}_{\log}(\mathbf{d}, e, f) = \sum_{n=1}^L a_n(e, f) \Phi_n(\mathbf{d}), \quad (3)$$

where the coefficients are estimated by solving a regularized least-squares problem:

$$\mathbf{a}(e, f) = \arg \min_{\mathbf{a}} \sum_{\mathbf{d}' \in \mathcal{D}_M} \|\hat{H}_{\log}(\mathbf{d}', e, f) - \Phi(\mathbf{d}')^\top \mathbf{a}\|_2^2 + \lambda \|\mathbf{a}\|_2^2, \quad (4)$$

where $\Phi(\mathbf{d}') = [\Phi_1(\mathbf{d}'), \dots, \Phi_L(\mathbf{d}')]^\top$, $\|\cdot\|_2$ denotes the Euclidean norm, and $\lambda \geq 0$ controls the regularization strength.

C. Learning-Based Methods

Learning-based methods utilize multi-subject datasets to improve HRTF upsampling performance and can be broadly categorized into coordinate-based models and sparse-to-dense regression models.

Coordinate-based models represent \hat{H}_{\log} as a continuous function of spatial direction (and optionally frequency):

$$\hat{H}_{\log}(\mathbf{d}, e, f) = \mathcal{F}_{\theta}(\mathbf{d}, f, z), \quad (5)$$

where \mathcal{F}_{θ} denotes a neural network with parameters θ , and z is a subject-specific embedding inferred from sparse

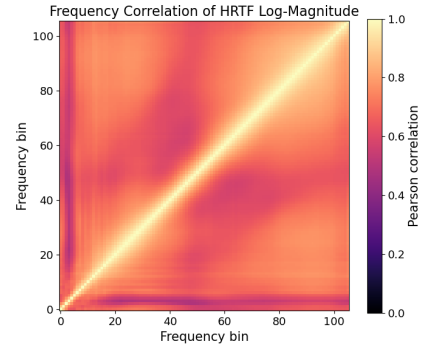


FIG. 2. Frequency-frequency Pearson correlation of HRTF log-magnitude responses. Each entry indicates the correlation between two frequency bins, computed over all subjects, directions, and ears. Strong correlations are observed both locally around the diagonal and across distant frequency bins.

measurements. In practice, the embedding captures individual characteristics, while spatial coordinates are provided as explicit inputs or conditioning variables to enable a continuous representation over the spherical domain.

By contrast, sparse-to-dense regression models directly map the target subject's sparse measurements to dense-direction HRTFs:

$$\hat{H}_{\log}(\mathbf{d}, e, f) = \mathcal{F}_{\theta}(\{\hat{H}_{\log}(\mathbf{d}', e, f)\}_{\mathbf{d}' \in \mathcal{D}_M}). \quad (6)$$

From a learning perspective, most neural network-based methods formulate HRTF upsampling as a supervised regression problem, where paired sparse and dense HRTF measurements are available during training. Given sparse observations, models are optimized to minimize the discrepancy between predicted and reference HRTFs.

A widely used metric for this purpose is the log-spectral distortion (LSD)⁴⁵, which quantifies differences between predicted and ground-truth log-magnitude spectra across spatial directions and frequency bins. In existing work, LSD is typically computed independently for each ear and then averaged across directions and subjects, and is employed either as a training loss or as an evaluation metric.

Despite their effectiveness, many learning-based approaches adopt architectural designs in which spatial generalization is explicitly modeled, whereas spectral information is processed in a largely implicit manner. This gap motivates the investigation of the frequency-domain feature modeling to capture the spectral structure better.

IV. PROPOSED METHOD

To motivate frequency-domain modeling, we first examine statistical dependencies between frequency bins in HRTF log-magnitude spectra. Fig. 2 shows the Pearson correlation matrix computed between pairs of fre-

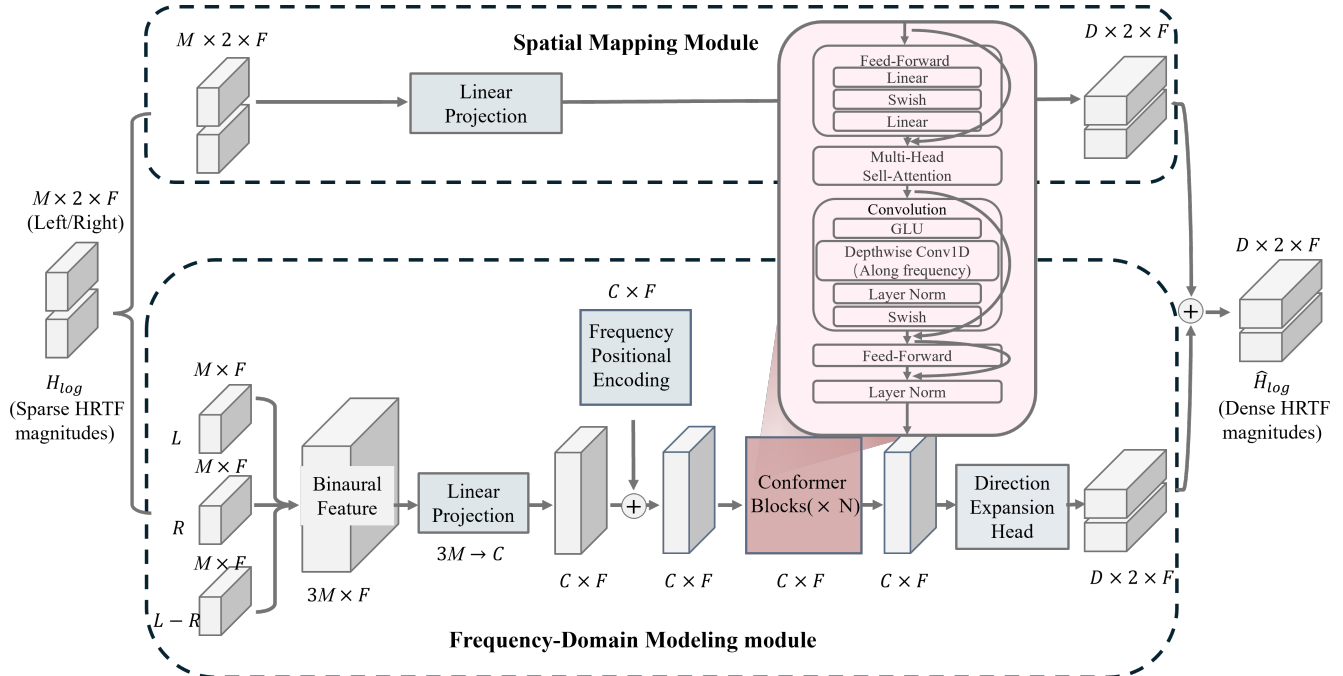


FIG. 3. Overall framework of the proposed FD-Conformer.

quency bins using log-magnitude responses averaged over all subjects, directions, and ears based on the SONICOM dataset. Strong spectral correlations are observed not only between neighboring frequencies but also across distant frequency bins, indicating the presence of both local spectral continuity and long-range frequency structure.

Motivated by this observation, we propose a frequency-domain neural architecture that explicitly models spectral dependencies along the frequency axis. The overall framework of the proposed neural network (FD-Conformer) is illustrated in Fig. 3. Given sparse measurements $H_{\log}(\mathbf{d}, e, f)$ at directions $\mathbf{d} \in \mathcal{D}_M$, the network takes input as a tensor $\mathbf{X} \in \mathbb{R}^{M \times 2 \times F}$, corresponding to M measured directions, two ears, and F frequency bins, and outputs the dense-direction HRTF log-magnitude tensor $\hat{H}_{\log} \in \mathbb{R}^{D \times 2 \times F}$, including predictions at U unmeasured directions.

A. Network Architecture

FD-Conformer employs a sparse-to-dense architecture comprising two modules: a Spatial Mapping module and a Frequency-Domain Modeling module. Both modules operate on the same sparse input and produce dense-direction estimates. The final prediction is obtained by summing the outputs of the two modules:

$$\hat{H}_{\log} = \hat{H}_{\log}^{\text{spatial}} + \hat{H}_{\log}^{\text{freq}}. \quad (7)$$

The Spatial Mapping module focuses on direction-wise information aggregation across sparse measurements, whereas the Frequency-Domain Modeling module captures spectral structure along the frequency dimension. Combining the outputs of the two modules enables effective utilization of both spatial and spectral information.

The Spatial Mapping module performs a direct sparse-to-dense mapping across directions using a linear transformation applied independently at each frequency bin. Given the input $\mathbf{X} \in \mathbb{R}^{M \times 2 \times F}$, this module produces an intermediate dense estimate $\hat{H}_{\log}^{\text{spatial}} \in \mathbb{R}^{D \times 2 \times F}$.

This module captures direction-dependent structure by aggregating information across sparse measurements, without introducing explicit modeling along the frequency dimension.

C. Binaural Spectral Representation

The Frequency-Domain Modeling module operates on a frequency-wise binaural spectral representation derived from the sparse input. For each frequency bin, three components are extracted from the sparse measurements: the left-ear magnitude (L), the right-ear magnitude (R), and their difference ($L - R$). These components are concatenated along the feature dimension, yielding a binaural spectral representation of dimension $3M$ per frequency bin.

Stacking the representations across all frequency bins results in a spectral feature map $\mathbf{S} \in \mathbb{R}^{3M \times F}$, which preserves binaural information while enabling explicit modeling along the frequency dimension.

D. Frequency-Domain Modeling with Conformer Blocks

The binaural spectral representation \mathbf{S} is first projected into a latent spectral space of dimension C via a learnable linear projection. Since the subsequent frequency-domain module is based on self-attention, which is permutation-invariant with respect to its inputs, a learnable frequency positional encoding⁴⁶ is added to \mathbf{S} to inject explicit frequency identity and ordering information. This encoding allows the model to distinguish between different frequency bins and to account for the physically meaningful ordering of frequencies when modeling spectral dependencies.

Let $\mathbf{H}^{(0)} \in \mathbb{R}^{F \times C}$ denote the resulting latent spectral representation. Frequency-domain modeling is performed using a stack of N Conformer blocks, which iteratively transform the features along the frequency axis:

$$\mathbf{H}^{(n)} = \text{ConformerBlock}\left(\mathbf{H}^{(n-1)}\right), \quad n = 1, \dots, N. \quad (8)$$

Each Conformer block comprises two feed-forward networks (FFN), a multi-head self-attention module (MHSA)⁴⁶, and a convolution module (Conv), connected via residual connections:

$$\mathbf{H}_1 = \mathbf{H}^{(n-1)} + \frac{1}{2} \text{FFN}\left(\mathbf{H}^{(n-1)}\right), \quad (9)$$

$$\mathbf{H}_2 = \mathbf{H}_1 + \text{MHSA}(\mathbf{H}_1), \quad (10)$$

$$\mathbf{H}_3 = \mathbf{H}_2 + \text{Conv}(\mathbf{H}_2), \quad (11)$$

$$\mathbf{H}_4 = \mathbf{H}_3 + \frac{1}{2} \text{FFN}(\mathbf{H}_3), \quad (12)$$

$$\mathbf{H}^{(n)} = \text{LayerNorm}(\mathbf{H}_4). \quad (13)$$

In the proposed setting, $\text{FFN}(\cdot)$ performs point-wise nonlinear transformations in the latent spectral space at each frequency bin. $\text{MHSA}(\cdot)$ captures long-range dependencies across frequency bins, which is useful for modeling global spectral structure in HRTF magnitudes. $\text{Conv}(\cdot)$ provides localized interactions along the frequency axis and is well suited for representing local spectral continuity and fine spectral details. Layer normalization (LayerNorm)⁴⁷ is applied to stabilize training and improve convergence. Together, these components enable joint modeling of local and long-range frequency-domain feature.

The output of the final Conformer block is mapped to dense-direction estimates through a direction expansion head, producing $\hat{\mathbf{H}}_{\log}^{\text{freq}} \in \mathbb{R}^{D \times 2 \times F}$. The final output $\hat{\mathbf{H}}_{\log}$ is obtained by summing this term with the output of the Spatial Mapping module, as defined in Eq. (7).

E. Training Objective

FD-Conformer is trained in a supervised manner. Following common practice in HRTF magnitude upsampling, the log-spectral distortion (LSD) is adopted as the primary training objective. LSD measures the discrepancy between the predicted and ground-truth log-magnitude spectra. For each direction \mathbf{d} and ear e , it is

defined as

$$\text{LSD}(\mathbf{d}, e) = \sqrt{\frac{1}{F} \sum_{f=1}^F (\hat{H}_{\log}(\mathbf{d}, e, f) - H_{\log}(\mathbf{d}, e, f))^2}, \quad (14)$$

where $H_{\log}(\mathbf{d}, e, f)$ and $\hat{H}_{\log}(\mathbf{d}, e, f)$ denote the ground-truth and predicted log-magnitude responses at frequency bin f , respectively. The overall LSD loss is obtained by averaging over both ears and all target directions,

$$\mathcal{L}_{\text{LSD}} = \frac{1}{2D} \sum_{e=1}^2 \sum_{\mathbf{d} \in \mathcal{D}} \text{LSD}(\mathbf{d}, e), \quad (15)$$

where \mathcal{D} denotes the set of dense directions. The loss is computed independently for each subject and then averaged across the training set.

While LSD provides a global measure of log-magnitude reconstruction accuracy averaged across frequencies, it treats individual frequency bins independently and does not explicitly constrain local spectral variation. As a result, sharp spectral features such as notches and peaks, which are important for elevation perception and front-back discrimination, may not be adequately preserved.

To complement the LSD objective, a spectral gradient loss (SGL) is introduced to constrain first-order spectral variations along the frequency axis. For each direction \mathbf{d} , ear e , and frequency bin f , the SGL is defined as

$$\text{SGL}(\mathbf{d}, e, f) = \left| \Delta_f \hat{H}_{\log}(\mathbf{d}, e, f) - \Delta_f H_{\log}(\mathbf{d}, e, f) \right|, \quad (16)$$

where

$$\Delta_f H_{\log}(\mathbf{d}, e, f) = H_{\log}(\mathbf{d}, e, f+1) - H_{\log}(\mathbf{d}, e, f) \quad (17)$$

denotes the spectral difference between adjacent frequency bins. The overall spectral gradient loss is obtained by averaging over directions, ears, and frequencies, i.e.,

$$\mathcal{L}_{\text{SGL}} = \frac{1}{2D(F-1)} \sum_{e=1}^2 \sum_{\mathbf{d} \in \mathcal{D}} \sum_{f=1}^{F-1} \text{SGL}(\mathbf{d}, e, f). \quad (18)$$

The total training objective is defined as

$$\mathcal{L} = \mathcal{L}_{\text{LSD}} + \beta \mathcal{L}_{\text{SGL}}, \quad (19)$$

where β is a weighting factor balancing the two terms. In this work, β is fixed to 1, assigning equal weight to the LSD and SGL components.

V. EXPERIMENTS

A. Dataset and Preprocessing

We evaluate the proposed method on the publicly available multi-subject HRTF dataset SONICOM²⁷ first. The SONICOM dataset contains HRIR measurements

from 200 subjects, each sampled at $D = 793$ directions. The HRIRs are recorded at 48 kHz and compensated using a minimum-phase free-field filter. Following the listener acoustic personalization (LAP) challenge protocol⁴⁸, each HRIR is transformed to the HRTF using a 256-point fast Fourier transform (FFT), and magnitudes within 187.5 Hz–19875 Hz are retained, yielding a 106-dimensional H_{\log} vector per ear. Sparse-to-dense upsampling is evaluated under four sparse measurement configurations with $M \in \{3, 5, 19, 100\}$. Consistent with the LAP challenge, we use the first 180 subjects for training and the remaining 20 for testing.

B. Experimental Setup

We use the Adam optimizer⁴⁹ with a learning rate of 1×10^{-3} and a batch size of 32. Training is performed for a maximum of 800 epochs for all experiments. The model checkpoint achieving the lowest validation LSD is selected for evaluation. During training, sparse measurements $H_{\log}(\mathbf{d}, e, f)$ for $\mathbf{d} \in \mathcal{D}_M$ are provided as input, and dense predictions are supervised using the full set of directions \mathcal{D} .

The FD-Conformer employs $L = 4$ Conformer blocks. Each block uses a model dimension of 128, a feed-forward dimension of 256, and 8 attention heads. The convolution module in each Conformer block adopts a kernel size of 7. The direction expansion head consists of a two-layer multilayer perceptron with a hidden dimension of 256. A dropout rate of 0.1 is applied throughout the frequency-domain branch. Learnable frequency positional encoding is enabled for all frequency-domain modeling variants unless explicitly stated otherwise.

C. Evaluation Metrics

We evaluate the upsampling accuracy using two perceptually relevant metrics: ILD error and LSD. Both metrics are computed from the ground-truth log-magnitude spectra $H_{\log}(\mathbf{d}, e, f)$ and the estimated spectra $\hat{H}_{\log}(\mathbf{d}, e, f)$.

The ILD is evaluated as a broadband measure that captures the overall interaural energy imbalance between the left- and right-ear responses. We adopt a broadband ILD formulation that is consistent with the time-domain ILD definition used in the LAP Challenge. The broadband energy at each ear is computed by summing the squared linear magnitudes across all frequency bins:

$$E(\mathbf{d}, e) = \sum_{f=1}^F \left| 10^{H_{\log}(\mathbf{d}, e, f)/20} \right|^2. \quad (20)$$

The broadband ILD for direction \mathbf{d} is then defined as the logarithmic ratio between the left- and right-ear broadband energies:

$$\text{ILD}(\mathbf{d}) = 10 \log_{10} \frac{E(\mathbf{d}, \text{Left})}{E(\mathbf{d}, \text{Right})}. \quad (21)$$

Similarly, the estimated ILD is given by

$$\hat{\text{ILD}}(\mathbf{d}) = 10 \log_{10} \frac{\hat{E}(\mathbf{d}, \text{Left})}{\hat{E}(\mathbf{d}, \text{Right})}. \quad (22)$$

The ILD error is computed as the mean absolute difference between the ground-truth and estimated ILD values over the unmeasured directions \mathcal{D}_U :

$$\Delta \text{ILD} = \frac{1}{U} \sum_{\mathbf{d} \in \mathcal{D}_U} \left| \text{ILD}(\mathbf{d}) - \hat{\text{ILD}}(\mathbf{d}) \right|. \quad (23)$$

The LSD is computed following Eq. (14) and averaged over both ears and the unmeasured directions:

$$\text{LSD} = \frac{1}{2U} \sum_{e=1}^2 \sum_{\mathbf{d} \in \mathcal{D}_U} \text{LSD}(\mathbf{d}, e). \quad (24)$$

All metrics are computed exclusively on the unmeasured directions \mathcal{D}_U , ensuring that the evaluation reflects upsampling performance rather than reconstruction of the measured inputs.

D. Frequency-Domain Modeling Analysis

This subsection analyzes the impact of different frequency-domain modeling strategies on HRTF magnitude upsampling. To ensure a fair comparison, all model variants share the same sparse-to-dense network architecture, including the Spatial Mapping module, binaural spectral representation, direction expansion head, training protocol, and evaluation metrics. The only difference between variants lies in the design of the frequency-domain modeling module highlighted by the red blocks in Fig. 3.

As a baseline, we first consider a model that relies solely on the Spatial Mapping module, without any explicit frequency-domain modeling. This variant serves as a reference for assessing the contribution of frequency-domain strategies. As reported in Table I, this spatial-only model consistently underperforms all frequency-aware variants. In extremely sparse settings (3 and 5 measurements), the LSD error is at least 1 dB higher than those with the frequency-domain modeling module, indicating the limitations of purely spatial upsampling.

1. Frequency-Domain Modeling Strategies

The upper part of Table I compares several frequency-domain modeling strategies under different sparsity levels. These strategies are organized according to their effective receptive field along the frequency axis, ranging from frequency-independent processing to joint local-global spectral modeling.

The per-frequency multilayer perceptron (MLP) processes each frequency bin independently and does not model inter-frequency dependencies. Despite its simplicity, this strategy already yields a noticeable improvement over the spatial-only baseline, indicating that frequency-wise nonlinear processing is beneficial even without explicit spectral context.

TABLE I. Exploration of frequency-domain modeling choices and ablation of the proposed Conformer-based model on the SONICOM dataset.

Model Variant	3 measurements		5 measurements		19 measurements		100 measurements	
	ILD [dB]	LSD [dB]	ILD [dB]	LSD [dB]	ILD [dB]	LSD [dB]	ILD [dB]	LSD [dB]
Spatial Mapping Only	2.42	5.83	1.39	5.91	0.88	3.59	0.45	2.39
Frequency-domain modeling strategies								
Per-frequency MLP	1.22	4.52	1.15	4.91	0.67	3.23	0.41	2.27
Vanilla Conv	0.98	4.16	1.15	4.51	0.65	3.15	0.40	2.27
Dilated Conv (expanded receptive field)	1.00	4.12	1.02	4.34	0.64	3.10	0.42	2.27
FD-Conformer (global + local)	0.94	3.97	0.97	4.00	0.65	3.08	0.41	2.27
Conformer component ablations								
w/o Conv	1.12	4.59	1.05	4.66	0.67	3.17	0.42	2.31
w/o Positional Encoding	0.96	4.08	1.02	4.12	0.66	3.09	0.41	2.31
w/o Spectral Gradient Loss	0.95	3.97	0.97	4.02	0.66	3.08	0.42	2.33

Convolutional models introduce local spectral interactions by mixing neighboring frequency bins with shared kernels, thereby enforcing short-range spectral continuity. Dilated convolution⁵⁰ further expands the effective receptive field, enabling the modeling of mid-range spectral correlations across frequency.

The FD-Conformer integrates convolution and self-attention mechanisms to jointly capture local spectral continuity and long-range frequency dependencies. Across all sparsity levels, models incorporating explicit frequency-domain interactions outperform frequency-independent baselines. The advantage is most pronounced in extremely sparse settings (3 and 5 measurements), where the FD-Conformer achieves the lowest LSD and ILD errors.

Both convolutional variants outperform the per-frequency MLP, confirming the benefit of explicit inter-frequency modeling. Dilated convolution generally improves upon standard convolution, particularly at moderate sparsity levels, suggesting that an expanded frequency receptive field is advantageous. However, neither convolutional variant consistently matches the performance of the FD-Conformer, indicating that fixed local kernels alone are insufficient to fully capture the non-stationary spectral characteristics of HRTF magnitudes.

As the number of sparse measurements increases, the performance gap between different frequency-domain modeling strategies gradually narrows. At 100 measurements, all methods achieve similar LSD values, implying that when sufficient directional information is available, the upsampling task becomes less sensitive to the specific choice of spectral modeling strategy.

2. Ablation of the FD-Conformer

The lower part of Table I presents an ablation study of the FD-Conformer to assess the contribution of its key components.

Removing the convolution module (*w/o Conv*) leads to a clear degradation in both LSD and ILD, particularly in the 3- and 5-measurement scenarios. While the self-attention mechanism remains capable of modeling long-range frequency dependencies, the absence of explicit local spectral interactions significantly degrades performance under extreme sparsity.

Removing the learnable frequency positional encoding (*w/o Positional Encoding*) primarily affects low-sparsity conditions, while having a negligible impact when more measurements are available. This suggests that explicit frequency identity information becomes more relevant when spectral structure must be inferred from very limited directional input.

Finally, removing the spectral gradient loss (*w/o Spectral Gradient Loss*) results in a modest performance decrease. This indicates that while gradient-based regularization can help constrain local spectral variation, the FD-Conformer architecture itself already provides strong frequency-domain structure through its combined convolutional and attention-based design.

Overall, these results highlight the importance of explicit frequency-domain modeling in low-sparsity HRTF upsampling, while its relative impact diminishes as more directional measurements become available.

E. Evaluation Results

Based on the architectural analysis presented in the previous section, we select the best-performing configuration of the proposed method, FD-Conformer, and compare it with existing approaches. The evaluated baselines include traditional interpolation methods, such as nearest-neighbor interpolation, barycentric interpolation, and spherical harmonics (SH), as well as learning-based methods including AE-GAN⁴¹ and RANF³⁵. Table II summarizes the quantitative results in terms of

TABLE II. SONICOM results: ILD and LSD errors for different numbers of sparse measurements.

Methods	3 measurements		5 measurements		19 measurements		100 measurements	
	ILD [dB]	LSD [dB]	ILD [dB]	LSD [dB]	ILD [dB]	LSD [dB]	ILD [dB]	LSD [dB]
Barycentric	7.50	8.56	4.54	8.33	1.76	4.79	0.55	3.20
Nearest neighbor	7.64	8.69	4.78	8.30	2.99	5.42	1.35	3.42
SH	6.05	9.96	5.44	10.35	1.68	5.43	0.44	3.38
AE-GAN ⁴¹	1.20	4.79	1.18	4.57	1.41	3.45	0.66	2.58
RANF ³⁵	1.21	4.41	1.31	4.46	0.97	3.63	0.78	3.02
FD-Conformer (Proposed)	0.93	3.97	0.97	4.00	0.65	3.08	0.41	2.27

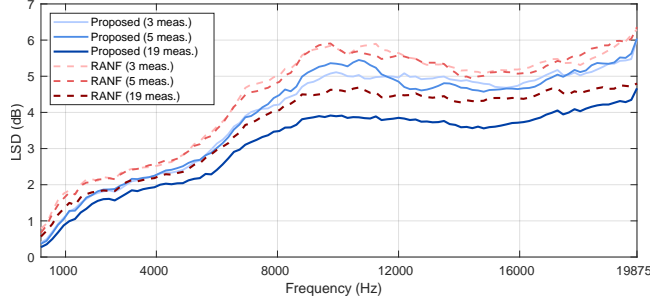


FIG. 4. Per-frequency LSD under different numbers of measurements.

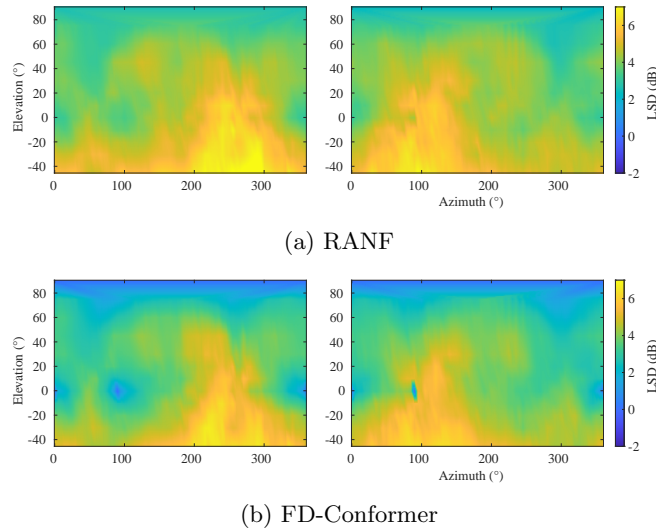


FIG. 5. Spatial distribution of LSD over azimuth and elevation under sparse measurements. For each method, the left and right panels correspond to the left and right ears, respectively.

ILD and LSD under different numbers of sparse measurements.

Traditional interpolation methods perform reasonably well when dense spatial sampling is available. In the 100-measurement setting, their LSD and ILD errors are

comparable to those of learning-based approaches. However, their performance rapidly degrades as the number of measurements decreases, due to sampling limitations and their reliance on within-subject interpolation only.

Across all sparsity levels, FD-Conformer consistently achieves the lowest ILD and LSD errors among all compared methods. In the extremely sparse setting with only three measured directions, FD-Conformer attains an LSD of 3.97 dB, significantly outperforming recent learning-based methods such as RANF (4.41 dB) and AE-GAN (4.79 dB), as well as all traditional baselines by a large margin. With five measurements, the performance advantage remains clear, with an LSD of 4.00 dB for FD-Conformer compared to 4.46 dB for RANF and 4.57 dB for AE-GAN.

As the number of available measurements increases, FD-Conformer continues to deliver consistent improvements. With 19 measured directions, it achieves an LSD of 3.08 dB, compared with 3.45 dB for AE-GAN and 3.63 dB for RANF. Even in the relatively dense setting with 100 measurements, FD-Conformer maintains the best performance, achieving an LSD of 2.27 dB.

The ILD results exhibit a similar trend. Despite the smaller numerical range of ILD errors, FD-Conformer consistently outperforms all baseline methods across all sparsity levels, indicating improved preservation of binaural level cues.

Figure 4 presents the per-frequency LSD under different numbers of sparse measurements. Across the entire frequency range, FD-Conformer consistently yields lower LSD than RANF for all sparsity levels. The performance gap is particularly pronounced in the mid- to high-frequency range (approximately 6–15 kHz), where HRTF magnitudes exhibit strong frequency-dependent structures such as pinna-induced resonances and spectral notches. As the number of sparse measurements increases from 3 to 19, the LSD curves of both methods decrease overall; however, FD-Conformer maintains a clear advantage, especially under extremely sparse conditions. This observation indicates that explicit frequency-domain modeling improves both overall spectral accuracy and robustness in frequency regions that are most sensitive to spectral distortion.

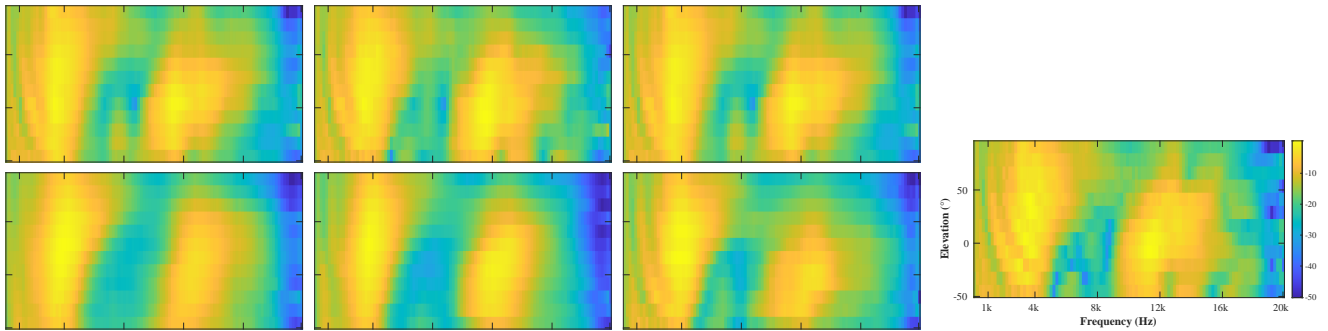


FIG. 6. Median-plane elevation–frequency spectra for the left ear of subject #200. Top row: proposed FD-Conformer with 3, 5, and 19 sparse directions. Bottom row: RANF with the same sparse configurations. Right: ground truth. All panels share the same frequency and elevation axes as well as the same color scale; for clarity, axes labels and the colorbar are shown only for the ground truth panel.

TABLE III. HUTUBS results: ILD and LSD errors for different numbers of sparse measurements.

Methods	6 measurements		14 measurements	
	ILD [dB]	LSD [dB]	ILD [dB]	LSD [dB]
IOA3D ¹¹	1.00	4.53	0.80	3.87
FD-Conformer	0.79	3.86	0.67	3.49

Figure 5 illustrates the spatial distribution of the LSD over azimuth and elevation under three sparse measurements, which is averaged over the whole frequency range. For both methods, larger reconstruction errors are consistently observed for source directions on the opposite side of the ear. Compared with RANF, the proposed FD-Conformer produces lower and more spatially homogeneous LSD values across most directions for both ears. Notably, regions with elevated reconstruction error are reduced and more spatially localized, demonstrating improved robustness and reconstruction fidelity.

Figure 6 visualizes the median-plane elevation–frequency spectra for a test subject (subject #200). The top row shows the results of FD-Conformer with 3, 5, and 19 sparse directions, while the bottom row presents the corresponding results obtained using RANF. The ground-truth spectrum is shown on the right for reference. Compared with RANF, FD-Conformer produces spectral patterns that more closely match the ground truth, particularly in the mid- and high-frequency regions. Under sparse measurement conditions, RANF exhibits noticeable spectral smearing and weakened notch structures, whereas FD-Conformer preserves sharper spectral transitions and more consistent elevation-dependent patterns. This qualitative comparison further supports the effectiveness of explicit frequency-domain modeling for reconstructing fine-grained HRTF spectral structure.

F. HUTUBS Dataset

To further assess the robustness of the proposed method under different measurement configurations, additional experiments are conducted on the HUTUBS dataset²⁶. Compared to SONICOM, HUTUBS differs in both spatial sampling density and measurement geometry, providing a complementary testbed for evaluating the generalization of the proposed architecture. The model is trained and evaluated separately on each dataset, and no cross-dataset transfer is performed.

The HUTUBS dataset contains HRIR measurements from 96 subjects, each sampled at 440 spatial directions. Following the same preprocessing pipeline as used for SONICOM, the HRIRs are resampled to 32 kHz, zero-padded to 256 samples, and transformed to the frequency domain using a 256-point FFT. We retain 128 magnitude bins per ear, resulting in a 128-dimensional H_{\log} representation. After removing duplicate entries, 94 subjects remain, of which 77, 10, and 7 are used for training, validation, and testing, respectively.

To ensure consistency with the SONICOM experiments, the proposed method is trained and evaluated on HUTUBS under the same experimental protocol. Sparse measurement subsets are generated using downsampled Lebedev grids with $M \in \{6, 14\}$.

As traditional interpolation-based methods exhibit trends similar to those observed on SONICOM, we focus here on comparisons with a representative learning-based method. Specifically, IOA3D¹¹ is included as a learning-based baseline in Table III to avoid redundancy and to highlight relative performance among data-driven methods.

As shown in Table III, the proposed method consistently achieves lower LSD errors than IOA3D across both sparsity levels. For ILD, performance differences between methods are smaller, which is expected given that ILD is generally less sensitive to spectral magnitude deviations than LSD. Overall, these results confirm that the benefits of explicit frequency-domain modeling extends beyond the SONICOM dataset, and the proposed

method remains robust under different spatial sampling patterns and dataset characteristics.

VI. CONCLUSION

This work investigated frequency-domain feature modeling for HRTF magnitude upsampling from sparse directional measurements. While existing learning-based methods have primarily focused on modeling spatial relationships across directions, the results demonstrate that the design of frequency-domain feature modeling plays an important role, particularly under extremely sparse measurement conditions. We proposed a sparse-to-dense framework that separates direct spatial mapping from frequency-domain modeling. Within this framework, a frequency-domain design space was explored, ranging from per-frequency MLPs and convolutional models to a Conformer-based architecture that jointly captures local spectral continuity and long-range frequency dependencies. Experiments on the SONICOM and HUTUBS datasets showed that progressively expanding the effective frequency receptive field leads to consistent performance improvements, with the Conformer-based model achieving the lowest ILD and LSD errors across all sparsity levels. These findings underscore the importance of frequency-aware modeling for HRTF magnitude upsampling and suggest that architectural choices along the frequency dimension should be regarded as a central design consideration, rather than an implementation detail. Future work will investigate tighter integration of frequency-domain modeling with spatial modeling, enabling joint learning of spectral and spatial structure.

ACKNOWLEDGMENTS

Computational facilities were provided by the UTS eResearch High Performance Computer Cluster.

REFERENCES

- ¹E. M. Wenzel and S. H. Foster, "Perceptual consequences of interpolating head-related transfer functions during spatial synthesis," in *Proceedings of IEEE Workshop on Applications of Signal Processing to Audio and Acoustics*, IEEE (1993), pp. 102–105.
- ²F. Keyrouz and K. Diepold, "Binaural source localization and spatial audio reproduction for telepresence applications," *PRES-ENCE: Teleoperators and Virtual Environments* **16**(5), 509–522 (2007).
- ³M. Geronazzo, S. Spagnol, and F. Avanzini, "Do we need individual head-related transfer functions for vertical localization? the case study of a spectral notch distance metric," *IEEE/ACM Transactions on Audio, Speech, and Language Processing* **26**(7), 1247–1260 (2018).
- ⁴R. Pelzer, M. Dinakaran, F. Brinkmann, S. Lepa, P. Grosche, and S. Weinzierl, "Head-related transfer function recommendation based on perceptual similarities and anthropometric features," *The Journal of the Acoustical Society of America* **148**(6), 3809–3817 (2020).
- ⁵J. Oberem, J.-G. Richter, D. Setzer, J. Seibold, I. Koch, and J. Fels, "Experiments on localization accuracy with non-individual and individual hrtfs comparing static and dynamic reproduction methods," *BioRxiv* 2020–03 (2020).
- ⁶T. McKenzie, D. T. Murphy, and G. Kearney, "Interaural level difference optimization of binaural ambisonic rendering," *Applied Sciences* **9**(6), 1226 (2019).
- ⁷A. Andreopoulou and B. F. Katz, "Identification of perceptually relevant methods of inter-aural time difference estimation," *The Journal of the Acoustical Society of America* **142**(2), 588–598 (2017).
- ⁸A. Carlini, C. Bordeau, and M. Ambard, "Auditory localization: a comprehensive practical review," *Frontiers in Psychology* **15**, 1408073 (2024).
- ⁹K. McMullen and Y. Wan, "A machine learning tutorial for spatial auditory display using head-related transfer functions," *The Journal of the Acoustical Society of America* **151**(2), 1277–1293 (2022).
- ¹⁰D. Fantini, M. Geronazzo, F. Avanzini, and S. Ntalampiras, "A survey on machine learning techniques for head-related transfer function individualization," *IEEE Open Journal of Signal Processing* (2025).
- ¹¹J. Zhao, D. Yao, and J. Li, "Head-related transfer function upsampling with spatial extrapolation features," *IEEE Transactions on Audio, Speech and Language Processing* (2025).
- ¹²V. Pulkki, "Virtual sound source positioning using vector base amplitude panning," *Journal of the audio engineering society* **45**(6), 456–466 (1997).
- ¹³D. R. Begault and L. J. Trejo, "3-d sound for virtual reality and multimedia," (2000).
- ¹⁴F. P. Freeland, L. W. Biscainho, and P. S. Diniz, "Interpositional transfer function for 3d-sound generation," *Journal of the Audio Engineering Society* **52**(9), 915–930 (2004).
- ¹⁵K. Hartung, J. Braasch, and S. J. Sterbing, "Comparison of different methods for the interpolation of head-related transfer functions," in *Proc. 16th Int. Audio Eng. Soc. Conf. Spatial Sound Reproduction*, (1999), pp. 319–329.
- ¹⁶M. Cuevas-Rodríguez, L. Picinali, D. González-Toledo, C. Garre, E. de la Rubia-Cuestas, L. Molina-Tanco, and A. Reyes-Lecuona, "3d tune-in toolkit: An open-source library for real-time binaural spatialisation," *PloS one* **14**(3), e0211899 (2019).
- ¹⁷D. N. Zotkin, R. Duraiswami, and N. A. Gumerov, "Regularized hrtf fitting using spherical harmonics," in *Proc. IEEE Workshop Appl. Signal Process. Audio Acoust.*, IEEE (2009), pp. 257–260.
- ¹⁸J. Ahrens, M. R. P. Thomas, and I. Tashev, "Hrtf magnitude modeling using a non-regularized least-squares fit of spherical harmonics coefficients on incomplete data," in *Proc. Asia Pacific Signal Inf. Process. Association Conf.*, IEEE (2012), pp. 1–5.
- ¹⁹C. Pörschmann, J. M. Arend, and F. Brinkmann, "Directional equalization of sparse head-related transfer function sets for spatial upsampling," *IEEE/ACM Transactions on Audio, Speech, and Language Processing* **27**(6), 1060–1071 (2019).
- ²⁰J. M. Arend, F. Brinkmann, and C. Pörschmann, "Assessing spherical harmonics interpolation of time-aligned head-related transfer functions," *Journal of the Audio Engineering Society* **69**(1/2), 104–117 (2021).
- ²¹B.-S. Xie, "Recovery of individual head-related transfer functions from a small set of measurements," *J. Acoust. Soc. Amer.* **132**(1), 282–294 (2012).
- ²²M. Zhang, Z. Ge, T. Liu, X. Wu, and T. Qu, "Modeling of individual hrtfs based on spatial principal component analysis," *IEEE/ACM Trans. Audio, Speech, Language Process.* **28**, 785–797 (2020).
- ²³K. Watanabe, Y. Iwaya, Y. Suzuki, S. Takane, and S. Sato, "Dataset of head-related transfer functions measured with a circular loudspeaker array," *Acoustical science and technology* **35**(3), 159–165 (2014).
- ²⁴R. Sridhar, J. G. Tylka, and E. Choueiri, "A database of head-related transfer functions and morphological measurements," in *Audio Engineering Society Convention 143*, Audio Engineering Society (2017).
- ²⁵C. Armstrong, L. Thresh, D. Murphy, and G. Kearney, "A perceptual evaluation of individual and non-individual hrtfs: A case

study of the sadie ii database," *Applied Sciences* **8**(11), 2029 (2018).

²⁶F. Brinkmann, M. Dinakaran, R. Pelzer, J. J. Wohlgemuth, F. Seipel, D. Voss, P. Grosche, and S. Weinzierl, "The hutubs head-related transfer function (hrtf) database," (2019).

²⁷I. Engel, R. Daugintis, T. Vicente, A. O. Hogg, J. Pauwels, A. J. Tournier, and L. Picinali, "The sonicom hrtf dataset," *Journal of the audio engineering society* **71**(5), 241–253 (2023).

²⁸Y. Ito, T. Nakamura, S. Koyama, and H. Saruwatari, "Head-related transfer function interpolation from spatially sparse measurements using autoencoder with source position conditioning," in *2022 International Workshop on Acoustic Signal Enhancement (IWAENC)*, IEEE (2022), pp. 1–5.

²⁹Y. Ito, T. Nakamura, S. Koyama, S. Sakamoto, and H. Saruwatari, "Spatial upsampling of head-related transfer function using neural network conditioned on source position and frequency," *IEEE Open Journal of Signal Processing* (2025).

³⁰B. Mildenhall, P. P. Srinivasan, M. Tancik, J. T. Barron, R. Ramamoorthi, and R. Ng, "Nerf: Representing scenes as neural radiance fields for view synthesis," *Communications of the ACM* **65**(1), 99–106 (2021).

³¹Y. Zhang, Y. Wang, and Z. Duan, "Hrtf field: Unifying measured hrtf magnitude representation with neural fields," in *Proc. IEEE Int. Conf. Acoust., Speech, Signal Process.*, IEEE (2023), pp. 1–5.

³²J. W. Lee, S. Lee, and K. Lee, "Global hrtf interpolation via learned affine transformation of hyper-conditioned features," in *ICASSP 2023-2023 IEEE International Conference on Acoustics, Speech and Signal Processing (ICASSP)*, IEEE (2023), pp. 1–5.

³³Y. Masuyama, G. Wichern, F. G. Germain, Z. Pan, S. Khurana, C. Hori, and J. L. Roux, "Niirf: Neural iir filter field for hrtf upsampling and personalization," arXiv preprint arXiv:2402.17907 (2024).

³⁴D. Hu, J. Hu, and C. Jiang, "Graph neural field with spatial-correlation augmentation for hrtf personalization," arXiv preprint arXiv:2511.10697 (2025).

³⁵Y. Masuyama, G. Wichern, F. G. Germain, C. Ick, and J. Le Roux, "Retrieval-augmented neural field for hrtf upsampling and personalization," in *ICASSP 2025-2025 IEEE International Conference on Acoustics, Speech and Signal Processing (ICASSP)*, IEEE (2025), pp. 1–5.

³⁶Z. Jiang, J. Sang, C. Zheng, A. Li, and X. Li, "Modeling individual head-related transfer functions from sparse measurements using a convolutional neural network," *J. Acoust. Soc. Amer.* **153**(1), 248–259 (2023).

³⁷A. O. Hogg, M. Jenkins, H. Liu, I. Squires, S. J. Cooper, and L. Picinali, "Hrtf upsampling with a generative adversarial network using a gnomonic equiangular projection," *IEEE/ACM Transactions on Audio, Speech, and Language Processing* **32**, 2085–2099 (2024).

³⁸X. Chen, F. Ma, Y. Zhang, A. Bastine, and P. N. Samarasinghe, "Head-related transfer function interpolation with a spherical cnn," arXiv preprint arXiv:2309.08290 (2023).

³⁹E. Thuillier, C. Jin, and V. Välimäki, "Hrtf interpolation using a spherical neural process meta-learner," *IEEE/ACM Transactions on Audio, Speech, and Language Processing* (2024).

⁴⁰X. Hu, J. Li, L. Picinali, and A. O. Hogg, "Hrtf spatial upsampling in the spherical harmonics domain employing a generative adversarial network," (2024).

⁴¹X. Hu, J. Li, L. Picinali, and A. O. Hogg, "Head-related transfer function upsampling using an autoencoder-based generative adversarial network with evaluation framework," *Audio Engineering Society* (2025).

⁴²V. R. Algazi, R. O. Duda, D. M. Thompson, and C. Avendano, "The cipic hrtf database," in *Proceedings of the 2001 IEEE Workshop on the Applications of Signal Processing to Audio and Acoustics (Cat. No. 01TH8575)*, IEEE (2001), pp. 99–102.

⁴³A. Gulati, J. Qin, C.-C. Chiu, N. Parmar, Y. Zhang, J. Yu, W. Han, S. Wang, Z. Zhang, Y. Wu, *et al.*, "Conformer: Convolution-augmented transformer for speech recognition," arXiv preprint arXiv:2005.08100 (2020).

⁴⁴D. S. Brungart and W. M. Rabinowitz, "Auditory localization of nearby sources: head-related transfer functions," *The Journal of the Acoustical Society of America* **106**(3), 1465–1479 (1999).

⁴⁵P. Gutierrez-Parera, J. J. Lopez, J. M. Mora-Merchan, and D. F. Larios, "Interaural time difference individualization in hrtf by scaling through anthropometric parameters," *Eurasip Journal On Audio, Speech, And Music Processing* **2022**(1), 9 (2022).

⁴⁶A. Vaswani, N. Shazeer, N. Parmar, J. Uszkoreit, L. Jones, A. N. Gomez, L. Kaiser, and I. Polosukhin, "Attention is all you need," *Advances in neural information processing systems* **30** (2017).

⁴⁷J. L. Ba, J. R. Kiros, and G. E. Hinton, "Layer normalization," arXiv preprint arXiv:1607.06450 (2016).

⁴⁸A. O. Hogg, R. Barumerli, R. Daugintis, K. C. Poole, F. Brinkmann, L. Picinali, and M. Geronazzo, "Listener acoustic personalisation challenge-lap24: Head-related transfer function upsampling," *IEEE Open Journal of Signal Processing* (2025).

⁴⁹D. P. Kingma and J. Ba, "Adam: A method for stochastic optimization," in *International Conference on Learning Representations (ICLR)* (2015).

⁵⁰F. Yu and V. Koltun, "Multi-scale context aggregation by dilated convolutions," arXiv preprint arXiv:1511.07122 (2015).